

Bonghun Shin, Soo Jeon, Jeongwon Ryu and Hyock Ju Kwon, “Compressed Sensing for Elastography in Portable Ultrasound,” *Ultrasonic Imaging*, **39**(6), pp. 393-413, Copyright © The Author(s) 2017. Reprinted by permission of SAGE Publications. Published version is available from <https://doi.org/10.1177/0161734617716938>.

Compressed Sensing for Elastography in Portable Ultrasound

Bonghun Shin^{1,#}, Soo Jeon¹, Jeongwon Ryu² and Hyock Ju Kwon¹

1. Department of Mechanical and Mechatronics Engineering, University of Waterloo, 200 University Ave. W., Waterloo, Ontario, Canada, N2L 3G1
2. Advanced Medical Technology Lab, Healcerion Co., Ltd, 38-21 Digital-ro, 31-gil, Guro-gu, Seoul, Korea

Corresponding Author: Bonghun Shin, Department of Mechanical and Mechatronics Engineering, University of Waterloo, 200 University Avenue West, Waterloo, Ontario, Canada N2L 3G1.

Tel: +1 519 888 4567 (ext) 31405, Fax: +1 519 885 5862

Email: bh3shin@uwaterloo.ca

Keywords

Compressive sensing; model basis; ℓ_1 minimization, Bayesian learning; elastography; elastograms; portable ultrasound; Doppler; strain estimation

Abstract

Portable wireless ultrasound has many advantages such as high portability, easy connectivity, strong individuality, as well as on-site diagnostic ability in real-time. Some of the modern portable ultrasound devices offer high image quality and multiple ultrasound modes comparable to console style ultrasound, however, none of them provides ultrasound elastography function that enables the diagnosis of malignant lesions using elastic properties. This is mainly due to the limitations of hardware performance and wireless data transfer speed for processing the large amount of data for elastography. Therefore, reduction of the data transfer size is one of the feasible solutions to overcome these limitations. Recently compressive sensing (CS) theory has been rigorously studied as a means to break the conventional Nyquist sampling rate and thus can significantly decrease the amount of measurement signals without sacrificing signal quality. In this research, we implemented various CS reconstruction frameworks and comparatively evaluated their reconstruction performance for realizing ultrasound elastography function on portable ultrasound. Combinations of three most common model bases (FT, DCT, and WA) and two reconstruction algorithms (ℓ_1 minimization and BSBL) were considered for CS frameworks. Two kinds of numerical phantoms, echoic and elastography phantoms, were developed to evaluate performance of CS on B-mode images and elastograms, respectively. To assess the reconstruction quality, mean absolute error (MAE), signal-to-noise (SNRe) and contrast-to-noise (CNRe) were measured on the B-mode images and elastograms from CS reconstructions. Results suggest that CS reconstruction adopting BSBL algorithm with DCT model basis can yield the best results for all the measures tested, and the maximum data reduction rate for producing readily discernable elastograms is around 60%.

Introduction

Ultrasound elastography (sonoelastography) [1, 2] is a non-invasive medical imaging modality that describes various elastic attribute of tissue to facilitate the detection of malignant legions. It is based on palpation principle that pathological lesions are normally stiffer than benign tissues; therefore, when they are compressed, strains in a malignant lesion are smaller than those in surrounding tissues. Several methods have been developed to calculate the strains, such as time-delay based [1], displacement-gradient based [2] and phase based [3] strain estimators. For example, in the time-delay strain estimation (TDE), strains are usually computed from the time delay generally obtained by cross-correlation of pre- and post-compression radiofrequency (RF) echo signals (Figure. 1), i.e.

$$\varepsilon_1 = \frac{(t_{1b} - t_{1a}) - (t_{2b} - t_{2a})}{t_{1b} - t_{1a}}, \quad (1)$$

where t_{1a} and t_{1b} are the arrival times of the pre-compression echoes from the two reference windows (proximal and distal), respectively, and t_{2a} and t_{2b} are the arrival times of the post-compression echoes from the same windows, respectively [1]. Its typical applications are to detect tumors in the breast [3, 4] and the prostate [5], to monitor thermal changes and ablation [6], to assess tendon motion [7], and to measure the stiffness of muscle and tendon [8, 9].

Recently, portable ultrasound is emerging as a new ultrasound imaging device, which is considerably smaller and lighter than the conventional console style ultrasound scanners,. Its high portability and mobility allow practitioners to make diagnostic and therapeutic decisions on site in real-time without having to take the patients out of their environment. This makes portable ultrasound an attractive medical modality particularly for harsh and remote sites [10].

Despite recent development of portable ultrasound devices capable of offering high image quality and multiple ultrasound mode, none of the current devices provide elastography function, mainly due to the limitations of hardware performance and data transfer speed of wireless communication. Note that conventional console style ultrasound devices perform large proportion of computations for elastography using dedicated hardware that is specially designed to process the substantial amount of ultrasound data acquisition (i.e. 192 channels of echo data with over 20 MHz sampling rate) and sophisticated image processing. Portable ultrasound devices, whereas, cannot call on dedicated hardware for such computation; instead, they have to depend on wireless-connected mobile device or laptop computer for image processing and elastography computation. Although computing power of portable computer has been increasing rapidly, it is still not comparable to that of dedicated hardware. Furthermore, the data transfer speed via wireless communication is insufficient to deliver a large amount of raw ultrasound RF echo data set that is needed to estimate strain fields and generate elastogram images.

One of the reasons requiring large amount of measurement data in conventional ultrasound is due to Shannon–Hartley theorem: the sampling rate must be at least twice the maximum frequency present in the recorded signal (the so-called Nyquist rate). When the Nyquist criterion is not met, i.e. sampling rate is less than twice signal frequency, it is known that a condition called aliasing occurs, which results in the differences between the original signal and a reconstructed data. In general, most ultrasound devices use around 4 times faster sampling rate than the minimum requirement of Nyquist rate in order to generate more accurate and higher resolution ultrasound images. Recently compressive sensing (CS) theory has been actively studied, as a means to overcome the limitation of

conventional Nyquist rate [11, 12] and enable the signal recovery with sparse representations from far fewer physical measurements than Nyquist rate. It has been typically exploited for the applications that need large amounts of signal acquisition processes such as dynamic MRI [13] or photoacoustic tomography (PAT) [14]. CS allows significant reduction of the measurement data, and thus of time for signal processing and data communication while maintaining output signal quality. Moreover, CS can reduce image artifacts and noise power when using the same number of measurements. Given all the benefits of CS, we hypothesize that CS could be a feasible solution to overcome the limitations of portable ultrasound in realizing elastography function. On the other hand, CS construction imposes a new computational load to the paired computing device (lab top or tablet PC); however, we also hypothesize that with the increase of computing power of such devices, the benefits of CS outweigh the disadvantages.

Note that although medical imaging may be one of the major areas that can be benefitted from CS, the adoption of CS in this field is relatively new [15]. Also, most of the related researches have been focusing on conventional pulse-echo B-mode imaging or suggesting several random sampling strategies [16], and none of them has attempted applying CS to elastography, particularly for portable ultrasound where reduction of measurement data that should be transferred through wireless communication is crucial. Therefore, the purpose of this research is to examine the feasibility of CS for elastography and to find the most efficient CS framework for implementing elastography function on portable ultrasound. Since the CS framework can also be used for B-mode reconstruction using subsampled RF data for reducing wireless communication data, the performance of the frameworks for reconstruction of B-mode images is also investigated. It needs to be

mentioned that the quality of CS reconstruction highly depends on sparsity representation of signal and reconstruction algorithms. Therefore, the research includes composing various CS frameworks associated with different model bases and reconstruction algorithms and assessing the quality of the B-mode images and elastograms from the RF data subsampled and reconstructed by each framework.

The paper is organized as follows. In the Background section, we review the CS theory and the major image reconstruction methods. A newly proposed strain estimation method so-called simple phase-based algorithm which is significantly faster than the conventional strain estimators is briefly introduced in this section. In the Method section, numerical phantoms developed for the virtual experiments are described and the various CS frameworks composed of several model bases and reconstruction algorithms are presented. Image quality measures for evaluating the results from each CS framework are also described. In the Results and Discussion section, the qualities of the images reconstructed by various CS frameworks are compared and the feasibility of the CS for implementing elastography function on portable ultrasound is discussed. Last section is devoted to the conclusion of this paper.

Background

Overview of Compressive Sensing Theory

CS enables the reconstruction of a signal $x \in \mathbb{R}^n$ with sparse representations from a small number of physical measurements $y \in \mathbb{R}^m, m < n$. The compressed measurement data y is acquired in the so-called sensing basis Φ , thus it can be mathematically expressed:

$$y = \Phi x \tag{2}$$

where Φ is an $m \times n$ matrix. Random Gaussian ensemble or Bernoulli matrices are often

used as a sensing basis Φ which is designed such that compressible signals x can be recovered exactly from the compressed data y .

Since most natural signals have concise representations when expressed in a convenient basis, the natural signals are usually significantly compressible [12]. Consider any signal $x \in R^n$ that can be represented in some model basis Ψ (where Ψ is an $n \times n$ matrix with ψ_1, \dots, ψ_n as column), which can be an orthonormal basis, a Fourier transform basis, or other basis depending on the measurement signal. The sparse representation of signal x is:

$$x = \sum_i^n v_i \psi_i = \Psi v \quad (3)$$

where v is an $n \times 1$ column vector and x and v are the same representation of a signal with x in the time domain and v in the Ψ domain. In the sparse representation, v has only $k < m < n$ non-zero coefficients (so-called k -sparse) and the signal x is a linear combination of just k basis vectors. By combining (2) and (3), the measurements can be written as:

$$y = \Phi \Psi v = A^{CS} v \quad (4)$$

where A^{CS} is an $m \times n$ matrix obeying a specified isometry constant, so called the restricted isometry property (RIP) [12]. In practice, the physical measurements are often corrupted by noise and the measurements with additive noise are rewritten as:

$$y = A^{CS} v + z \quad (5)$$

where z is a deterministic or stochastic unknown error term and bounds the amount of noise in the data ($\|z\|_{l_2} \leq \epsilon$). As a solution for finding the optimal values of v in (5), two classes of the optimization algorithms have been mainly employed to reconstruct the optimal values of sparse signal v ; the first one uses deterministic algorithms including ℓ_1 minimization (L1) algorithms [11], and the other uses stochastic algorithms using Bayesian

learning framework such as block sparse Bayesian learning (BSBL) [16, 17].

In the L1 approaches, reconstruction can be first performed by solving the following minimization problem [12], given by:

$$P: \hat{v} = \underset{v \in \mathbb{R}^n}{\operatorname{argmin}} \|v\|_{l_1} \text{ subject to } \|y - A^{CS}v\|_{l_2} \leq \epsilon \quad (6)$$

In solving (6), a sparse reconstruction algorithm estimates the optimal values of v in (5), and then the signal x can be computed from (3).

On the other hand, the unknown sparse signal v can also be reconstructed by exploiting the principle of Bayesian inference as a stochastic algorithm. In this approach, a priori probability density functions (pdf's) are associated with each of the unknown variables v , and the Bayes law is used to find the posteriori probability to be maximized, such that:

$$p(v|y) \propto p(y|v)p(v) \quad (7)$$

where $p(y|v)$ represents the likelihood and $p(v)$ contains prior information about the unknown sparse v . Assume that the A^{CS} matrix is known and the noise z is approximated by an additive Gaussian noise with zero mean and unknown variance σ^2 . Then the sparse coefficients v and the noise variance σ^2 are the quantities of CS estimate based on Bayesian framework. The associated Gaussian likelihood model is given by [17]:

$$p(y|v, \sigma^2) = (\pi\sigma^2)^{-n} \exp\left(-\frac{1}{\sigma^2} \|y - A^{CS}v\|_{l_2}^2\right) \quad (8)$$

By introducing an a priori on the coefficients to be recovered, the sparsity model is modeled as follows:

$$p_0(v) \propto \exp(-\|v\|_{l_0}) \quad (9)$$

Now, CS transformed the recovery problem of the sparse coefficients v into a linear-regression problem with the prior constraint by the Bayesian approach.

Block Sparse Bayesian learning (BSBL) algorithms have been proposed to further

improve reconstruction performance of wireless electrocardiogram (ECG) applications [16, 18]. By exploring and exploiting the intra-block correlation that correlates the entries in each block, the recovery performance of BSBL was greatly improved compared to other methods ignoring the intra-block correlation. The BSBL algorithms also have a pruning mechanism in which they use a threshold to prune out some irrelevant coefficient. Recently, several BSBL algorithms such as BSBL Expectation Maximization (BSBL-EM), BSBL Bound-Optimization (BSBL-BO) and BSBL-L1 have been proposed [19]. In this work, BSBL-BO [19] which is known to have balanced performance and speed is selected to show the CS reconstruction performance in generating elastography for portable ultrasound.

Model bases

CS performance strongly depends on signal sparsity representation in the model basis Ψ [17]; however, since the raw RF data in ultrasound show the oscillatory pattern, it is not trivial to find the adequate sparsity representation with any basis. In this study, we considered three types of model basis: wave atom (WA), discrete cosine transform (DCT), and discrete Fourier transform (FT).

WA basis recently proposed by Demanent and Ying [20] describes the exact relationship between the directional wavelets and the Gabor transform (a special case of the short-time Fourier transform). Consequently, it produces a multiscale transform with frame elements indexed by scale, location, and orientation parameters. The multiscale feature in WA is useful for adapting to arbitrary local directions of oscillatory patterns [17]. Meanwhile, DCT expresses a finite sequence of data points in terms of a sum of cosine functions (real-valued) oscillating at different frequencies, while FT represents a

sum of scaled-and-shifted vector in the complex frequency domain.

Simple Phase-based Strain Estimation

The axial strain of a segment that has been deformed along loading direction is defined as

$$\varepsilon = \frac{\Delta L}{L} = \frac{L - L_0}{L_0} \quad (10)$$

where ΔL is the difference between the final length L and initial length L_0 of the segment.

In elastography, it can be assumed that an ultrasonic transducer transmits waves toward an object moving with an instantaneous velocity V as depicted in Figure 2. If a segment is defined as the region of axial length L_0 , and the change in the length of the segment $\Delta L = T_{PR}(V_2 - V_1)$ (Figure 2), the axial strain can be rewritten as

$$\varepsilon = \frac{T_{PR}}{L_0}(V_2 - V_1) \quad (11)$$

where the corresponding velocity V_i at both endpoints of the segment is evaluated by 2D autocorrelator [21, 22] and is expressed as

$$\hat{V}_i = \frac{c}{2} \frac{T_s}{T_{PR}} \frac{\arg\{\gamma_i[0,1]\}}{\arg\{\gamma_i[1,0]\}} = \frac{c}{2} \frac{T_s}{T_{PR}} \Gamma_i \quad (12)$$

where $\arg\{\gamma_i[1,0]\}$ and $\arg\{\gamma_i[0,1]\}$ are the phase of autocorrelation at lags in sampling interval and pulse repetition period, respectively.

Now let us consider an axial segment along single scan line. If the segment is centered at m depth samples with the upper and lower endpoints given by $m_1 = m - \Delta m/2$ and $m_2 = m + \Delta m/2$, the axial length of the segment is

$$L_0 = \Delta m \frac{c}{2} T_s \quad (13)$$

where the tunable parameter Δm controls the length of the axial length of the segment. By substituting Eq. (13) into (11) and rewriting V_1 and V_2 using Eq. (12), the local axial strain

can be simplified as

$$\varepsilon = \frac{\Gamma_2 - \Gamma_1}{\Delta m} \quad (14)$$

where Γ_1 and Γ_2 are the 2D autocorrelation values at both endpoints of the segment.

Note that Eq. (14) contains only segment length Δm and the phase angle Γ at the upper and lower end points of the segment; thus, it is not affected by sampling intervals along the depth (T_s) and the frame (T_{PR}). In portable ultrasound, sampling interval along the frame (T_{PR}) refers to the time interval to make a pair of RF data sets from the tissue before and after the physical compression. This time interval (equivalent to pulse repetition period) is also equivalent to data-dumping interval via Wi-Fi network established between portable ultrasound and the paired computing device; therefore, the sampling interval cannot be uniform or stable as that of console-style scanner. However, Eq. (14) indicates that although data dumping interval is not consistent, strain estimation accuracy is not degraded in the SPSE method.

In this study, CS is applied to portable ultrasound following the procedure as illustrated in Figure 3. First, a pair of original RF data sets are collected and compressed by the portable US device (Figure 3, above). The undersampled (compressed) RF data sets are then transmitted to a laptop or mobile device through the Wi-Fi network established between them. The laptop computer (or mobile device) recovers the compressed data sets and generates the elastogram using the SPSE method (Figure 3, bottom).

Methods

Numerical Phantoms

Numerical phantoms were developed to perform the virtual ultrasound experiment to evaluate the performance of various CS frameworks on image reconstruction. Two types of numerical phantoms were modeled: echoic and elastography phantoms.

An echoic phantom contains arrays of hyperechoic and hypoechoic inclusions [17] to assess the performance of CS on the recovery of B-mode images. Using Field II [23, 24], an open-source Matlab-based ultrasound simulation code, RF signals from a numerical phantom of size $50 \times 10 \times 55 \text{ mm}^3$ were simulated. A 192-element linear array probe with the center frequency 3.5 MHz was modeled to generate the regular ultrasound B-mode images. The numerical phantom was composed of a total of 100,000 point scatterers, four hyperechoic, and four hypoechoic inclusions of the diameter of 6 mm. The hyperechoic inclusions mimicked the malignant tumour with round hyperdensities (BiRads 4 or 5), while hypoechoic inclusions simulated benign cysts filled with liquid without any scatterers (BiRads 1 or 2). The standard deviation of the scatterers' amplitude distribution inside the hyperechoic inclusions was ten times that of the background. The spatial distribution of the scatterers in the hyperechoic inclusions and the background was modeled as uniform and the amplitude of these regions followed a zero mean Gaussian distribution, respectively.

An elastography phantom was constructed by combining finite element analysis (FEA) model and Field II code. Using commercial FEA code (Abaqus/CAE 6.10) (Figure 4, upper left), a linear elastic phantom of the size $40 \times 50 \times 10 \text{ mm}^3$ was modeled to have a stiff cylindrical inclusion (10 mm) in the soft matrix. The FEA model was meshed with

approximately 427,000 3D quadratic tetrahedron elements and 77,000 nodes. The elastic moduli of the matrix and the inclusion were set to 20 kPa and 100 kPa, respectively, mimicking a carcinoma in breast tissue. Poisson's ratio of 0.49 was applied to the whole phantom. The vertical movement of the bottom surface of the phantom was constrained while 0.1% axial compressive strain was applied to the top surface. The coordinates of each node were determined and recorded by FEA as the deformation field data sets. Then Field II code was used to add random scatterers to the nodal displacements and generate the corresponding pre- and post-deformation RF signal data (Figure 4, upper center). The amplitudes of the random scatterers were kept constant throughout the phantom, thus the inclusion could not be detected in the RF signal or in the B-mode image. In order to simulate the portable ultrasound device, a linear probe having 152 ultrasound elements and 24 active elements was virtually modeled with Field II. The center frequency of the transducer was placed at 3.5 MHz and the sampling rate of RF signals was set to 28 MHz. The speed of sound through the phantom was set to 1,540 m/s. With this setting, Field II generated 128 simulated RF lines (A-lines) with each line containing 2,589 samples across the phantom depth. Parameters for both echoic and elastography phantoms are listed in Table 1. The simple phase-based strain estimator (SPSE) was applied to the RF data sets from CS reconstruction (Figure 4, upper and lower right) and the strain fields were estimated from the reconstructed RF dataset (Figure 4, lower center). The differences between the strain estimates and the true strains computed by the FEM were regarded as estimation errors (Figure 4, lower left).

Model Bases

In order to find a relevant sparse representation of the raw RF data in ultrasound,

reconstruction performance of the CS adopting WA, DCT, and FT model bases were compared. Since the elastogram used in this study depicts the axial strain field, each basis function is applied to one-dimensional RF signal, and then the measurement signal x is converted to the sparse representation v in the Ψ domain as described in Eq. (2). For WA model base, the WA package based on [20] was employed to conduct the forward and inverse WA transform. For DCT and FT, one-dimensional built-in function sets in Matlab were utilized, with the signal segment size set to 256 for all model bases.

Reconstruction Algorithms

The simulated RF data sets produced from the numerical elastography phantom were subsampled by removing 10%-80% of the original samples using a uniform random law. For example, 70% subsampling rate suggests that 70% of the original samples are removed and only 30% are maintained in the compressed vector y . CS reconstruction was then performed on the subsampled RF data by solving the CS minimization problem in Eq. (5). Two types of optimization algorithms were adopted: ℓ_1 minimization (L1) and BSBL. In the L1 experiments using the ℓ_1 -Magic package [25], signal segment size, the number of maximum iteration were set to 0.003, 256, and 50, respectively. BSBL, a recently proposed stochastic-based reconstruction algorithm, was also implemented by using the BSBL-BO package [19]. In the BSBL experiments, the segment length and block size, the accuracy threshold ϵ , and the maximum iteration were set to 256, 12, $1e-8$ and 7, respectively. During the experiment, both methods successfully solved the reconstruction problem without any stability issue.

Image Quality Measures

The accuracy of the B-mode and elastograms images from CS reconstruction were

quantified by comparing them with the images from the original data through the mean absolute error (MAE) given by

$$MAE = \frac{1}{N} \sum_{i=1}^N |I_{o_i} - I_{r_i}| \quad (15)$$

where N is the total number of the image data, I_{o_i} and I_{r_i} are the intensities of both original and reconstructed images, respectively.

The image quality of elastograms were examined using the signal-to-noise ratio (SNRe) and the contrast-to-noise ratio (CNRe). Specifically, the elastographic SNRe identifying the quantitative measurement of the accuracy and the precision of an elastogram is defined as [26]

$$SNRe = \frac{m_s}{\sigma_s} \quad (16)$$

where m_s is the mean value of the strain, and σ_s is the standard deviation of the measured strain. The elastographic CNRe is an important parameter to determine the detectability of a stiff lesion in an elastogram and is defined as [27]

$$CNRe = \frac{2(m_o - m_i)^2}{\sigma_o^2 + \sigma_i^2} \quad (17)$$

where $m_i, m_o, \sigma_i^2,$ and σ_o^2 are the mean values and the variance values for the inside (subscript i) and the outside (subscript o) of the lesion, respectively.

Results and Discussion

Evaluation of B-mode reconstruction

B-mode images the produced from the RF data reconstructed by various CS frameworks, combining either of two reconstruction algorithms (L1 and BSBL) with one of three model bases (FT, DCT and WA), respectively, were evaluated as shown in Figure 5 and 6 to demonstrate the general CS application in medical ultrasound. To compare the quality of reconstructed B-mode images, we selected 50% subsampling rate which is reasonably applicable to generate the elastograms.

As for the echoic phantom containing four hyper- and hypoechoic inclusions (Figure 5), both L1 (Figure 5(a)) and BSBL (Figure 5(b)) algorithms could recover the detailed patterns of the phantom, and their hyper- and hypoechoic inclusions are clearly discernable, except the framework combining L1 with FT basis (L1-FT). Among the B-mode images reconstructed by L1 (Figure 5(a)), both L1-DCT and L1-WA show comparable image quality and similar MAE values of 0.082 dB. L1-FT produces the lowest image quality with the highest MAE value (0.242 dB). Hyper- and hypoechoic inclusions on L1-FT image are blurred and dispersed, which make them hardly discernable. On the other hand, B-mode images reconstructed by BSBL present better image quality and lower MAE than those by L1, as shown in Figure 5(b). BSBL-DCT produces the lowest MAE of 0.022 dB, while the MAEs of BSBL-FT and BSBL-WA are slightly higher at 0.029 and 0.037 dB, respectively.

B-mode images of the elastography phantom containing a stiff inclusion from various CS frameworks are shown in Figure 6. Since the standard deviation of the scatterers' amplitude distribution is the same as that of background, the inclusion is not visible on the

B-mode images. Among the B-mode images reconstructed by L1 (Figure 6(a)), both L1-DCT and L1-WA are associated with the same level of MAE at 0.066 dB, whereas L1-FT yields the highest MAE of 0.111 dB with unexpected vertical black patterns appearing on the reconstructed image. Whereas, B-mode images reconstructed by the BSBL (Figure 6(b)) preserve the patterns intact with excellent accordance with the original image. Comparing MAE values associated with the same model bases, BSBL-based frameworks yield much lower values than L1-based ones. Among the BSBL images in Figure 6(b), BSBL-FT is associated with the lowest MAE of 0.017 dB, followed by BSBL-DCT and BSBL-WA with the MAE of 0.022 and 0.034 dB, respectively.

Plots of MAE values for various CS frameworks are presented in Figure 7 as a function of removed data (subsampling rate) from 10% to 80%. Quite consistently, the errors increase with the number of samples removed, for all CS frameworks. As for the echoic phantom (Figure 7(a)), the MAE values are linearly increasing until 50% subsampling for all model bases, and then rapidly rising except for L1-FT that shows linearly increasing trend and much higher values than the other two bases. It is also notable that BSBL-based frameworks yield lower MAE values than L1-based ones with little effects from model bases, which is consistent with the trends in B-mode images (Figure 5 and 6). The MAE plots for L1-DCT and L1-WA are almost equivalent, while all BSBL-based plots agree well with each other. In case of elastography phantom (Figure 7(b)), the trends of MAE are similar to those of the echoic phantom except L1-FT which is still higher than the others, but follows much closer trend than that in echoic phantom. Over all MAE values associated with BSBL-based frameworks are lower than those of L1-based ones with little effect from model bases.

Evaluation of Elastograms

By applying the SPSE method to the RF data of elastography phantom from CS reconstruction, elastograms are generated to describe the strain fields under compressive deformation. Image quality of the elastograms from various CS frameworks are comparatively investigated.

The elastograms from L1-based frameworks for the subsampling rate from 30% to 50% are compared in Figure 8. The elastograms for all bases for 30% subsampling rate preserve the original patterns very well, and the stiff inclusion in the center is clearly discernable. At 40% subsampling rate (Figure 8(b)), both L1-DCT and L1-WA elastograms still show discernable inclusion and consistent matrix strain which are close to the original image, while degradations in the inclusion and the matrix start occurring in L1-FT elastogram. When the subsampling rate is increased to 50% (Figure 8(c)) the shapes of the stiff inclusion for all three bases are hardly discernable and the strain fields in the matrix show inconsistent and locally varying behavior. Over all, L1-DCT and L1-WA preserve the strain patterns of similar quality until 40%, while L1-FT tends to lose the patterns much earlier than the others. From the observation, 40% subsampling rate seems to be the threshold compression ratio to effectively detect the inclusion for the elastograms from L1-based CS frameworks.

Strain values measured along the vertical centerline across the L1-based elastograms are plotted in Figure 9. The strain fields for three bases over the subsampling rate from 30% to 50% are compared with the strains from the FEA as a ground truth. At 30% subsampling rate (Figure 9(a)), both plots from L1-DCT and L1-WA show good agreement with the FEA strains. For 40% (Figure 9(b)), L1-DCT and L1-WA still follow the trend of

FEA, but the strains start oscillating both in the inclusion and the matrix where strains are regarded as constant. The oscillations in these regions are significantly amplified with further increase of subsampling rate (Figure 9(c)). Beyond 50%, the strain plots become too noisy to identify the shape of the inclusion, which also indicates that sampling rate around 40% should be the threshold for L1-based CS frameworks.

The elastograms from BSBL-based CS frameworks over the subsampling rate from 50% to 70% are presented in Figure 10. At 50% subsampling rate (Figure 10(a)), all elastograms preserve the patterns superbly; they are almost equivalent to the original elastogram and accurately depict strain distribution in the inclusion and the matrix. At 60%, the inclusion is still discernable, regardless of slight strain degradation particularly in BSBL-WA (Figure 10(b)). Beyond 70% subsampling rate, all elastograms are significantly degraded and the original strain patterns are lost almost completely as shown in Figure 10(c). Qualitative observation suggests that BSBL-DCT elastograms best agree with the original ones, particularly for 50% and 60% subsampling rate.

The strain plots along the vertical centerline across the BSBL-based elastograms are presented in Figure 11. The strain plots for all three bases show excellent agreement with the ground truth (FEA results) for 50% subsampling rate (Figure 11(a)). With the increase of subsampling rate, reconstructed strain plots start to show oscillating behavior (Figure 11(b)). Eventually, all strain plots lose the track of the ground truth beyond 70% subsampling rate, as shown in Figure 11(c). It can be summarized that that BLBL-based CS reconstruction is highly reliable until 50%, and is reasonably accurate up to 60% subsampling rate, for all three bases tested. Furthermore, the qualities of elastograms from BSBL-based CS frameworks are far less influenced by the model bases than those from

L1-based ones.

Evaluation of Image Quality Measures and Computation Times

Image qualities of the elastograms are evaluated with three image quality measures (MAE, SNRe, and CNRe) to determine the optimal CS scheme for generating the ultrasound elastograms. All the image measures are collected over the subsampling rate from 10% to 80%.

The MAE plots of elastograms (Figure 12) from various CS frameworks are compared with the reference strain error (black solid line) that corresponds to 15% of the applied strain (0.1%). The reference error plays as the error criterion based on the observation that MAE plots rise rapidly once they reach this level. Since MAE can be regarded as monotonic function of subsampling rate, the threshold subsampling rate of each framework is estimated from the intersection between the MAE and the error criterion.

Among the MAE plots for L1-based frameworks (dashed lines in Figure 12), the L1-FT yields the highest error level and intersects the error criterion at around 33% subsampling rate, while L1-DCT and L1-WA are slowly increasing until 40% subsampling rate from which they start rising rapidly. Overall, among L1-based frameworks, L1-WA presents the best result until it reaches the error criterion.

All BSBL-based CS frameworks generate similar level of MAE lower than error criterion until 50%, regardless of associated model bases. Threshold subsampling rate is identified to be around 60% for BSBL-WA and BSBL-FT and around 63% for BSBL-DCT. The comparison between L1- and BSBL-based plots in Figure 12 suggest that BSBL-based CS frameworks yield more reliable results than L1-based ones. Particularly BSBL-DCT yields the lowest error level over the subsampling range tested.

The elastographic SNRe and CNRe identifying the precision and the discernibility of the elastograms are quantified in Figure 13. All SNRe plots in Figure 13(a) present slowly decreasing trend at first, but start to drop rapidly with increase of subsampling rate. BSBL-based frameworks yield higher SNRe than L1-based ones across all subsampling range tested. In Figure 13(b), CNRe plots from CS frameworks are almost equivalent to those from original elastogram (meaning excellent discernibility) in low subsampling range; however, they start to drop rapidly with increase of subsampling rate. Over all, both SNRe and CNRe plots from BSBL-based frameworks present higher values than those from L1-based ones over the entire subsampling range. Furthermore, results from BSBL-based frameworks are less influenced by the model bases because its block-wise approach might maximize the signal sparsity of ultrasound echo signal. All the image quality measures (MAE, SNRe, and CNRe) imply that the feasible level of the subsampling rate without significant loss of patterns is 40% for L1-based and 60% for BSBL-based frameworks, respectively.

Computation times of the CS reconstruction methods were also measured on a Windows 10 computer (2.3MHz, i7-3670 CPU with 12 GB RAM, ASUS-K55VD) using the in-house developed Matlab code. Overall, L1-WA showed the fastest computation time (16.732 seconds) while L1-FT spent 105.909 seconds due to the calculation of its complex array. On the other hand, BSBL-based frameworks presented relatively similar computation times among different bases. BSBL-WA took only 38.454 seconds, while BSBL-DCT and BSBL-FT recorded 41.864 and 55.479 seconds, respectively. As for the number of average iterations, L1-FT recorded 42.61, while L1-DCT and L1-WA took 12.95 and 12.73 iterations, respectively. For the BSBL-based frameworks, all methods

required around 7 iterations. Threshold subsampling rates and the corresponding MAEs, SNRe, CNRe, and computation times for different CS frameworks are summarized in Table 2.

Conclusion

Large amount of ultrasound echo data to be transferred through wireless communication is one of the major limitations in implementing ultrasound elastography function on portable ultrasound. As a means to reduce the size of the measurement data, this paper address the feasibility of applying compressive sensing (CS) method to elastography. Since CS reconstruction performance is highly affected by model basis representing the sparse expansion of the data, as well as reconstruction algorithm to solve the minimization problem, we tested three bases, discrete Fourier transform (FT), discrete cosine transform (DCT), and the recently introduced wave atoms (WA), and two reconstruction algorithms, ℓ_1 minimization (L1) and Block sparse Bayesian learning (BSBL).

The quality of the reconstructions was quantified using the B-mode and elastogram images of simulated numerical phantoms through three image quality measures, mean absolute error (MAE), signal-to-noise ratio (SNRe) and contrast-to-noise ratio (CNRe) at varying subsampling rates. The results indicate that BSBL-based CS frameworks generally delivered the superior performance to L1-based ones. Particularly the CS framework adopting BSBL-DCT combination yielded the lowest MAE and the highest SNRe and CNRe among all combinations, and possibly the optimal CS reconstruction framework for elastography. The results also suggest that the maximum data reduction (subsampling) rate for generating reasonable elastograms is 60% for BSBL-DCT framework.

Future work will consist in extending the CS reconstruction in real-time. Currently the

computation for CS reconstruction is so heavy that real-time processing is hard to be achieved. Improving the algorithm for efficient and fast computation is essential to the application of CS to portable ultrasound. Another important improvement involves investigating other reconstruction algorithms and model bases, specifically adapted to ultrasound RF data. Such improvement would make it possible to build an even sparser representation than current BSBL-DCT combination thus allows better reconstruction for a given subsampling rate.

Acknowledgements

The work was supported by Natural Sciences and Engineering Research Council of Canada (NSERC).

References

1. Ophir J, Cespedes I, Ponnekanti H, et al. Elastography: a quantitative method for imaging the elasticity of biological tissues. *Ultrason Imag.* 1991;13(2):111-134.
2. Ophir J, Srinivasan S, Righetti R, et al. Elastography: a decade of progress (2000-2010). *Curr Med Imag Rev.* 2011;7(4):292-312.
3. Han Y, Kim DW, Kwon HJ. Application of digital image cross-correlation and smoothing function to the diagnosis of breast cancer. *J Mech Behav Biomed Mater.* 2012;14:7-18.
4. Shin B, Gopaul D, Fienberg S, Kwon HJ. Application of Eshelby's Solution to Elastography for Diagnosis of Breast Cancer. *Ultrason Imag.* 2016;38(2): 115-36.
5. Lorenz A, Sommerfeld H-J, Garcia-Schürmann M, et al. A new system for the acquisition of ultrasonic multicompression strain images of the human prostate in vivo. *IEEE Trans Ultrason Ferroelect Freq Contr.* 1999; 46(5): 1147-1154.
6. Rivaz H, Fleming I, Assumpcao L, et al. Ablation monitoring with elastography: 2D in-vivo and 3D ex-vivo studies. In: *Med Image Comput Computer-Assisted Intervention–MICCAI, Berlin Heidelberg, Germany, 6 Sep 2008*, pp. 458-466.
7. Chernak LA, Thelen DG. Tendon motion and strain patterns evaluated with two-dimensional ultrasound elastography. *J Biomech.* 2012;45(15):2618-2623.
8. Brandenburg JE, Eby SF, Song P, et al. Ultrasound elastography: the new frontier in direct measurement of muscle stiffness. *Arch Phys Med Rehabil.* 2014;95(11):2207-2219.
9. Muraki T, Ishikawa H, Morise S, Yamamoto N, et al. Ultrasound elastography-based assessment of the elasticity of the supraspinatus muscle and tendon during muscle contraction. *J Shoulder Elb Surg.* 2015;24(1):120-126.

10. Nelson BP, Sanghvi A. Out of hospital point of care ultrasound: current use models and future directions. *Eur J Trauma Emergency Surg.* 2016;42(2):139-150.
11. Candes EJ, Romberg J, Tao T, Robust uncertainty principles: exact signal reconstruction from highly incomplete frequency information, *IEEE T Inform Theory.* 2006;52:489-509.
12. Candes EJ, Wakin MB, An Introduction To Compressive Sampling, *IEEE Signal Proc Mag.* 2008;25:21-30.
13. Mollenbach S and Jensen J. Duplex scanning using sparse data sequences. In *Proc IEEE Ultrason Symp.*, Nov. 2008, pp. 5-8.
14. Guo Z, et al. Compressive sensing in photoacoustic tomography in vivo. *J Biomed Opt.* 2010; doi:10.1117/1.3381187.
15. Liebgott H, Basarab A, Kouame D, Bernard O, Friboulet D. Compressive sensing in medical ultrasound. In *2012 IEEE Int Ultrason Symp 2012 Oct 7*, pp. 1-6.
16. Balouchestani M, Raahemifar K, Krishnan S. New sampling approach for wireless ECG systems with compressed sensing theory. In *Med Meas Appl P (MeMeA), 2013 IEEE Int Symp on 2013 May 4*, pp. 213-218.
17. Liebgott H, Prost R, Friboulet D. Pre-beamformed RF signal reconstruction in medical ultrasound using compressive sensing. *Ultrason.* 2013 Feb 28;53(2):525-33.
18. Zhang Z, Jung T, Makeig S, Rao B. Compressed sensing for energy-efficient wireless telemonitoring of noninvasive fetal ECG via block sparse Bayesian learning. *IEEE T Biomed Eng.* 2013;60(2):300-309.
19. Zhang Z, Rao B. "Extension of SBL algorithms for the recovery of block sparse signals with intra-block correlation. *IEEE T Signal Process.* 2013;61(8): 2009-2015.

20. Demanet L, Ying L. Wave atoms and sparsity of oscillatory patterns. *Appl Comput Harmon A*. 2007;23:368-387.
21. Loupas T, Powers JT, Gill RW. An axial velocity estimator for ultrasound blood flow imaging, based on a full evaluation of the dropper equation by means of a two-dimensional autocorrelation approach. *IEEE Trans Ultrason Ferroelect Freq Contr*. 1995;42(4):672-688.
22. Loupas T, Gill RW. Multifrequency Doppler: Improving the Quality of Spectral Estimation by Making Full Use of the Information Present in the Backscattered RF Echoes. *IEEE Trans Ultrason Ferroelect Freq Contr*. 1994;41(4):522-531.
23. Jensen JA, Svendsen NB. Calculation of pressure fields from arbitrarily shaped, apodized, and excited ultrasound transducers. *IEEE Trans Ultrason Ferroelect Freq Contr*. 1992; 39(2): 262-267.
24. Jensen JA. Field: A program for simulating ultrasound systems. In 10th Nordic-Baltic Conf on Biomed Imag. 1996; Vol. 34, Suppl. 1, Part 1:351-353
25. Candes E, Romberg J. l1-magic: Recovery of sparse signals via convex programming (2005). URL: <http://statweb.stanford.edu/~candes/l1magic/downloads/l1magic.pdf>.
26. Céspedes I, Ophir J. Reduction of image noise in elastography. *Ultrason Imag*. 1993;15(2):89-102.
27. Ophir J, Alam SK, Garra B, et al, Varghese T. Elastography: ultrasonic estimation and imaging of the elastic properties of tissues. *Proc Inst Mech Eng, Part H: J Eng Med*. 1999;213(3):203-233.

Figure captions

Figure 1. Schematic of the principle of time-delay strain estimation method.

Figure 2. Principle of strain estimation in SPSE: ultrasonic transducer transmits waves toward a segment (left). The lower (farthest away from the transducer) and upper endpoints of the segment are moving with an instantaneous velocity V_2 and V_1 , respectively (right). As a result, the segment length L_0 at $t = T_0$ is changed to L at $t = T_0 + T_{PR}$.

Figure 3. Schematic of the CS procedure for generating elastogram in portable US device.

Figure 4. Schematic of the procedure to construct a virtual elastography phantom and to produce elastogram from the undersampled RF data of the phantom using CS reconstruction.

Figure 5. B-mode images of the echoic phantom containing hyper- and hypo- echoic inclusions produced from the original data and the reconstructed data by (a) L1-based and (b) BSBL-based CS reconstruction frameworks, combined with FT, DCT, and WA model bases, respectively. Data were reconstructed using 50% subsampling.

Figure 6. B-mode images of the elastography phantom produced from the original data and the reconstructed data by (a) the L1-based and (b) the BSBL-based based CS reconstruction frameworks, combined with FT, DCT, and WA model bases, respectively. Data were reconstructed using 50% subsampling.

Figure 7. MAE plots associated with various CS frameworks as functions of subsampling rate, measured on: (a) the echoic phantom, (b) the elastography phantom.

Figure 8. Elastograms of elastography phantom computed from the original data and from various CS reconstruction frameworks for the subsampling rate of: (a) 30%, (b) 40%, and (c) 50%.

Figure 9. Strain values measured along the vertical centerline across the elastograms computed from the L1-based CS reconstruction frameworks for the subsampling rate of: (a) 30%, (b) 40%, (c) 50%. The FEA plots are the ground truth.

Figure 10. Elastograms of the elastography phantom computed from the original data and from the BSBL-based CS reconstruction frameworks for the subsampling rate of: (a) 30%, (b) 40%, and (c) 50%.

Figure 11. Strain values measured along the vertical centerline across the elastograms computed from the BSBL-based CS reconstruction frameworks for the subsampling rate of: (a) 50%, (b) 60%, (c) 70%.

Figure 12. MAE of the elastograms as a function of subsampling rate. The error is computed on the elastograms produced from the various CS reconstruction frameworks. Reference error is 15% of the applied strain.

Figure 13. (a) SNRe and (b) CNRe of the elastograms as a function of subsampling rate. The image quality measures are computed on the elastograms produced from the original data and from various CS reconstruction frameworks.

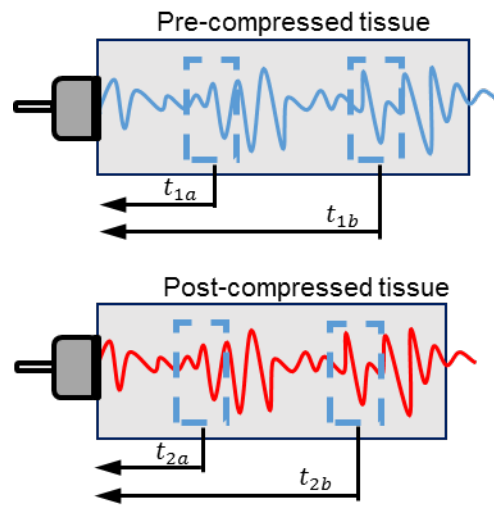


Figure 1. Schematic of the principle of time-delay strain estimation method.

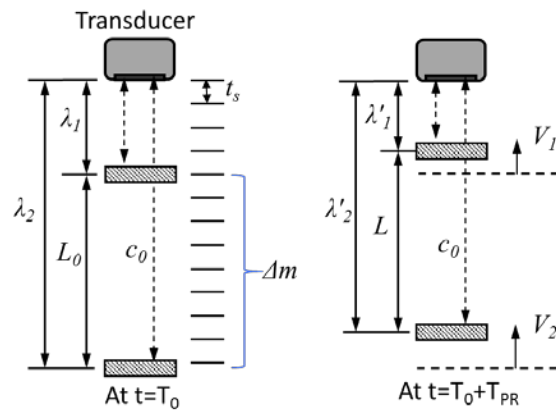


Figure 2. Principle of strain estimation in SPSE: ultrasonic transducer transmits waves toward a segment (left). The lower (farthest away from the transducer) and upper endpoints of the segment are moving with an instantaneous velocity V_2 and V_1 , respectively (right). As a result, the segment length L_0 at $t = T_0$ is changed to L at $t = T_0 + T_{PR}$.

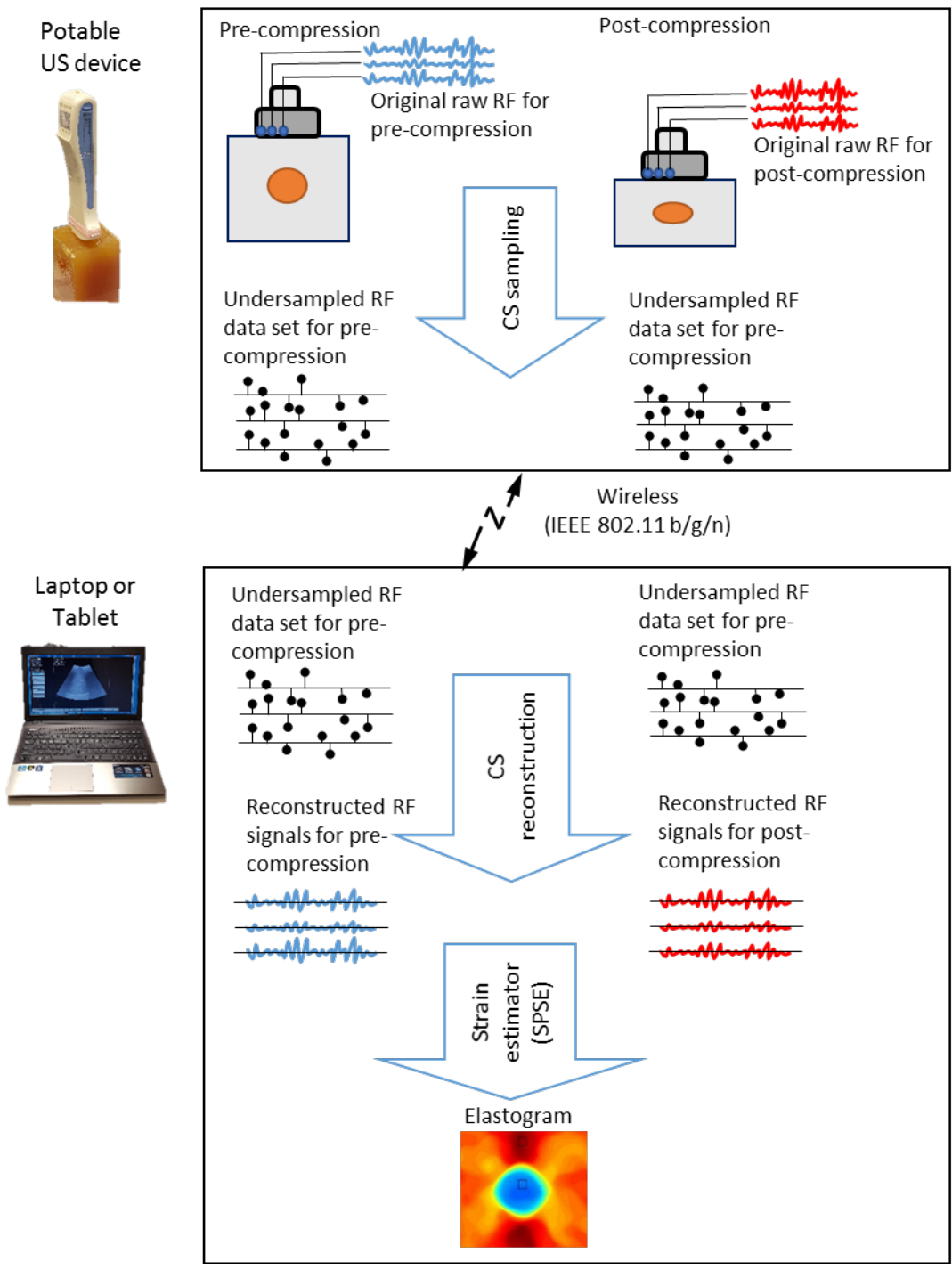


Figure 3. Schematic of the CS procedure for generating elastogram in portable US device.

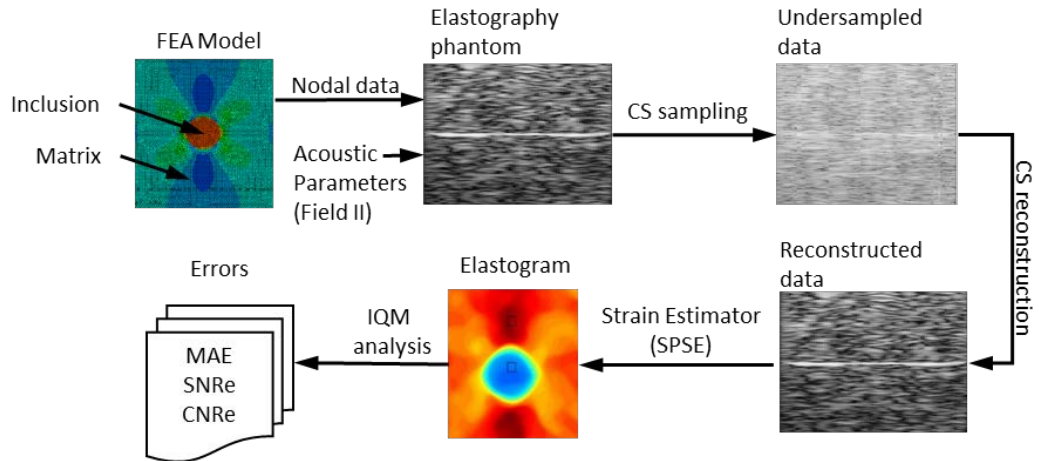
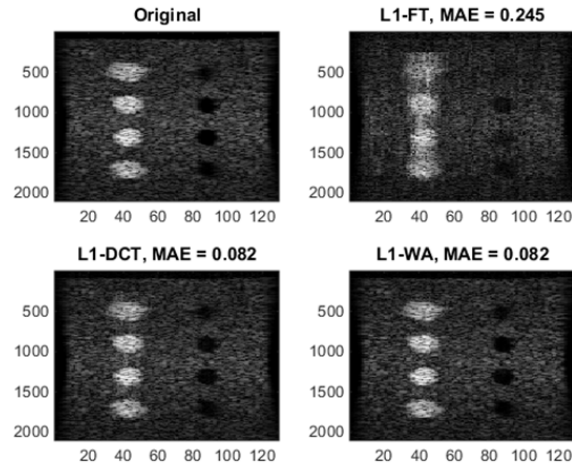
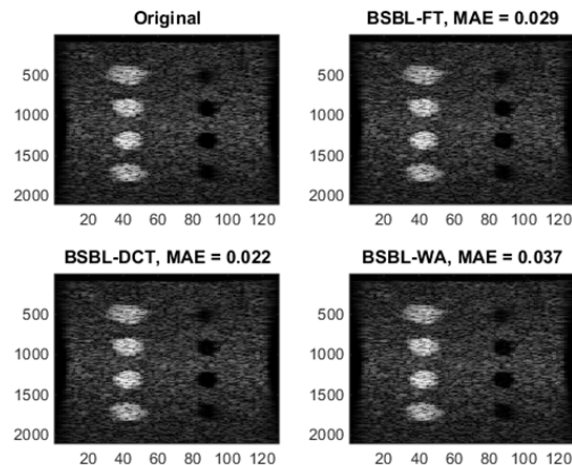


Figure 4. Schematic of the procedure to construct a virtual elastography phantom and to produce elastogram from the undersampled RF data of the phantom using CS reconstruction.

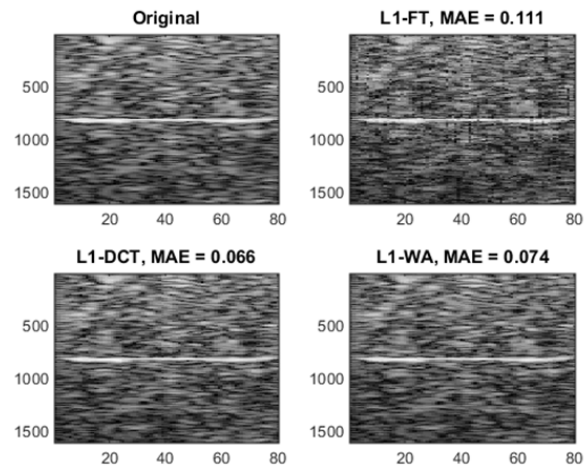


(a)

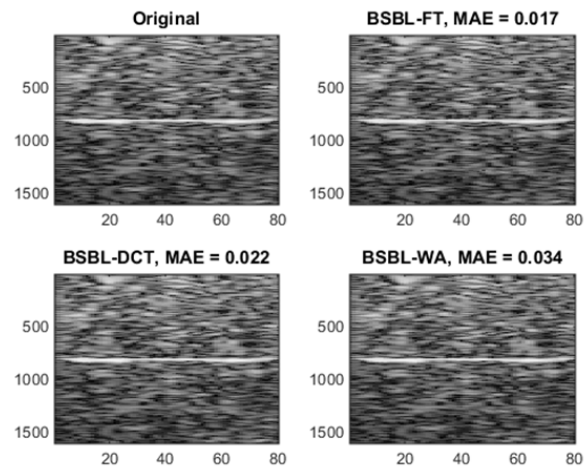


(b)

Figure 5. B-mode images of the echoic phantom containing hyper- and hypo-echoic inclusions produced from the original data and the reconstructed data by (a) L1-based and (b) BSBL-based CS reconstruction frameworks, combined with FT, DCT, and WA model bases, respectively. Data were reconstructed using 50% subsampling.

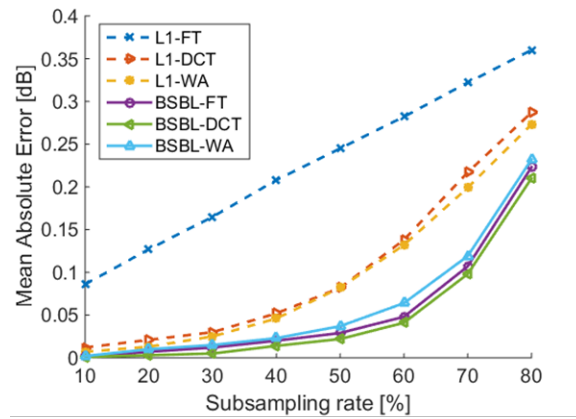


(a)

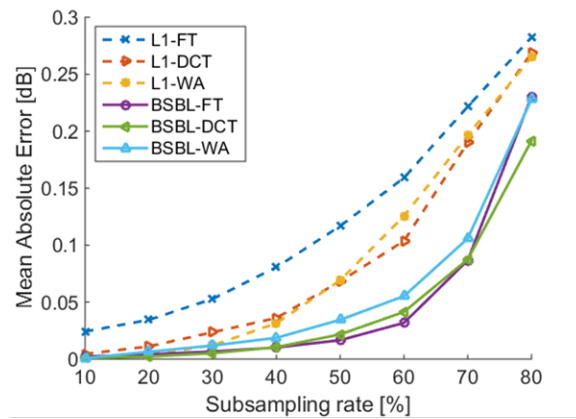


(b)

Figure 6. B-mode images of the elastography phantom produced from the original data and the reconstructed data by (a) the L1-based and (b) the BSBL-based based CS reconstruction frameworks, combined with FT, DCT, and WA model bases, respectively. Data were reconstructed using 50% subsampling.



(a)



(b)

Figure 7. MAE plots associated with various CS frameworks as functions of subsampling rate, measured on: (a) the echoic phantom, (b) the elastography phantom.

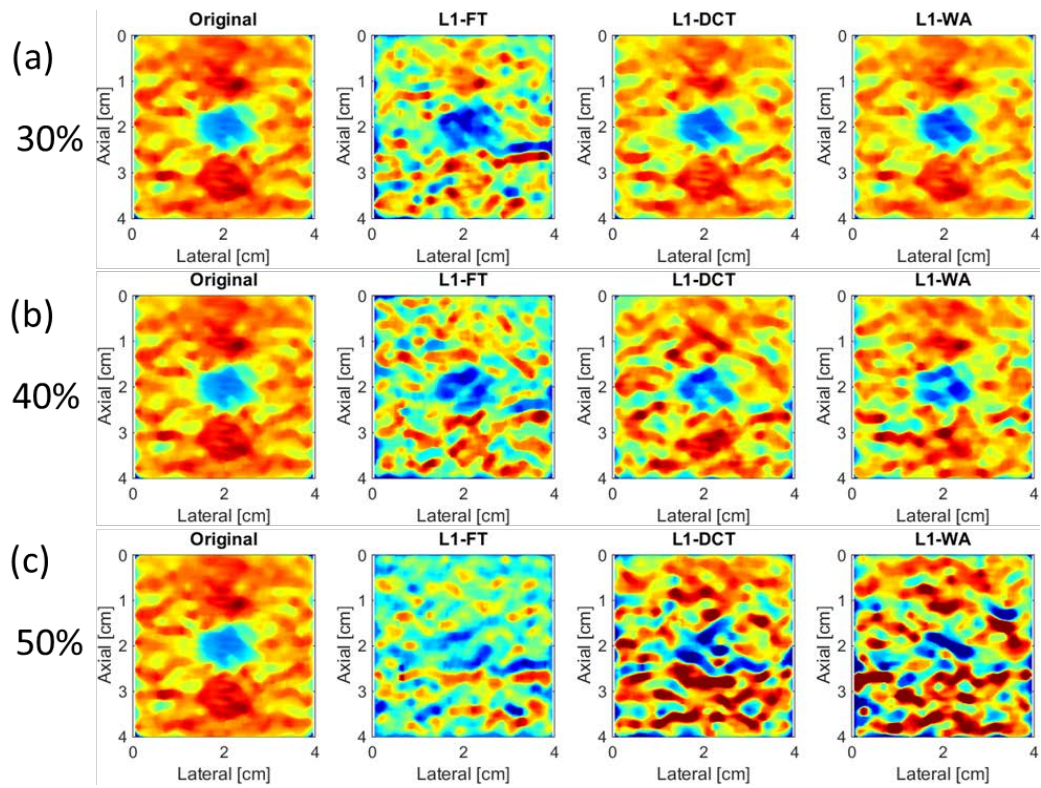


Figure 8. Elastograms of elastography phantom computed from the original data and from various CS reconstruction frameworks for the subsampling rate of: (a) 30%, (b) 40%, and (c) 50%.

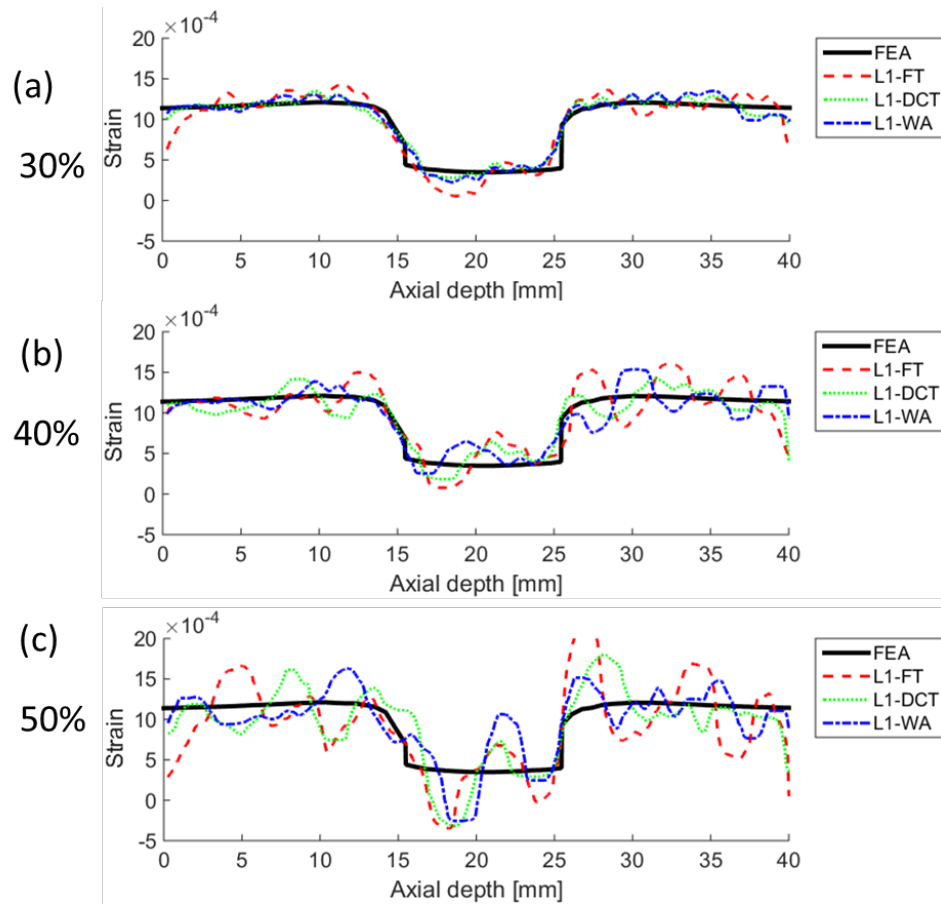


Figure 9. Strain values measured along the vertical centerline across the elastograms computed from the L1-based CS reconstruction frameworks for the subsampling rate of: (a) 30%, (b) 40%, (c) 50%. The FEA plots are the ground truth.

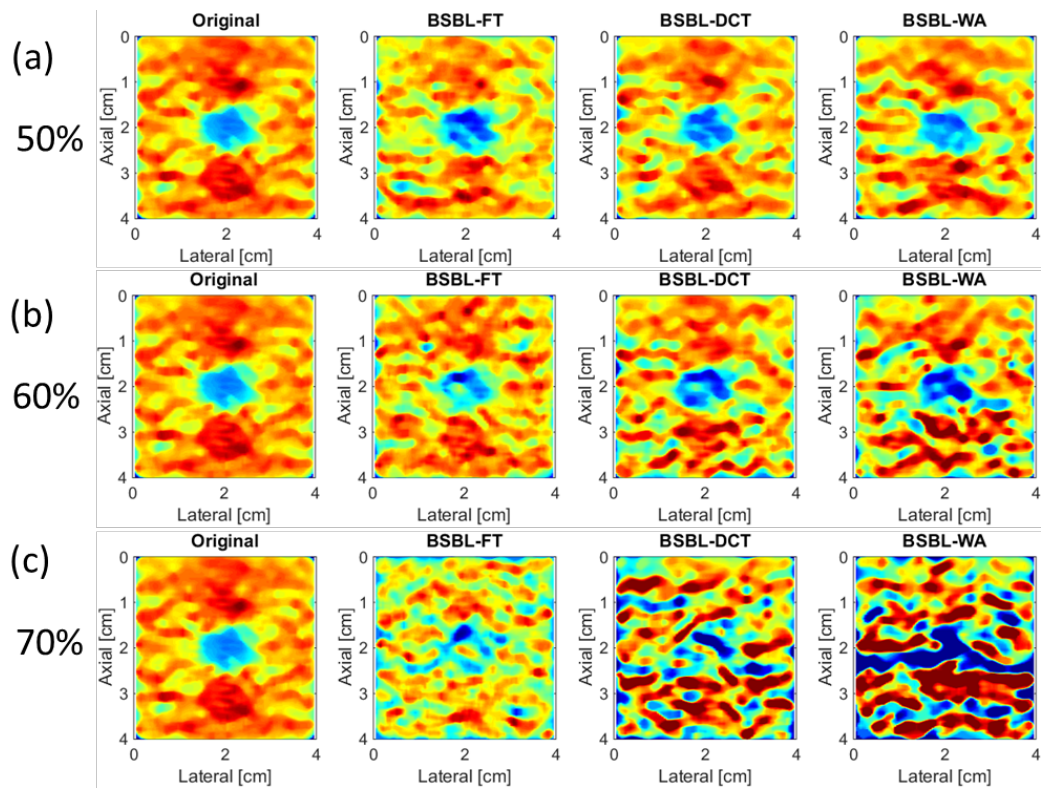


Figure 10. Elastograms of the elastography phantom computed from the original data and from the BSBL-based CS reconstruction frameworks for the subsampling rate of: (a) 30%, (b) 40%, and (c) 50%.

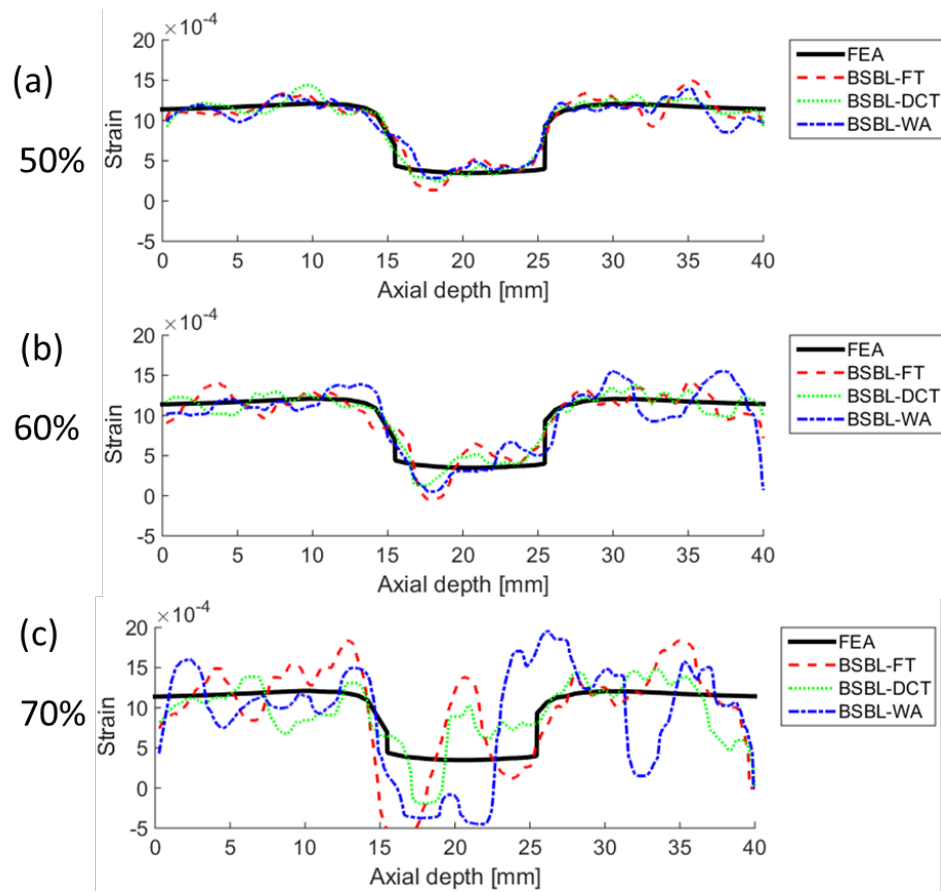


Figure 11. Strain values measured along the vertical centerline across the elastograms computed from the BSBL-based CS reconstruction frameworks for the subsampling rate of: (a) 50%, (b) 60%, (c) 70%.

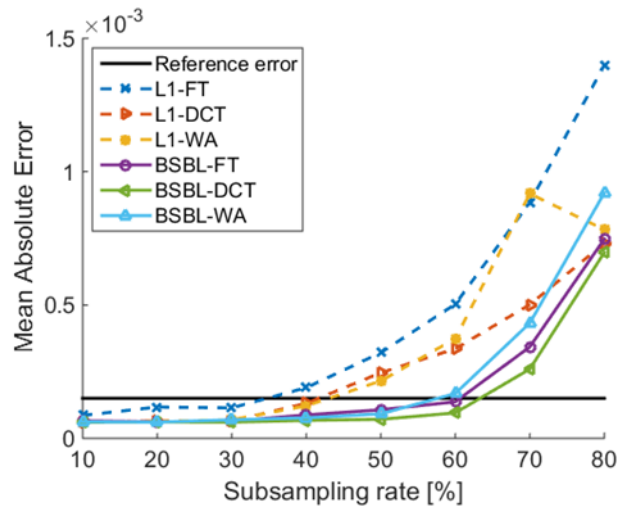


Figure 12. MAE of the elastograms as a function of subsampling rate. The error is computed on the elastograms produced from the various CS reconstruction frameworks. Reference error is 15% of the applied strain.

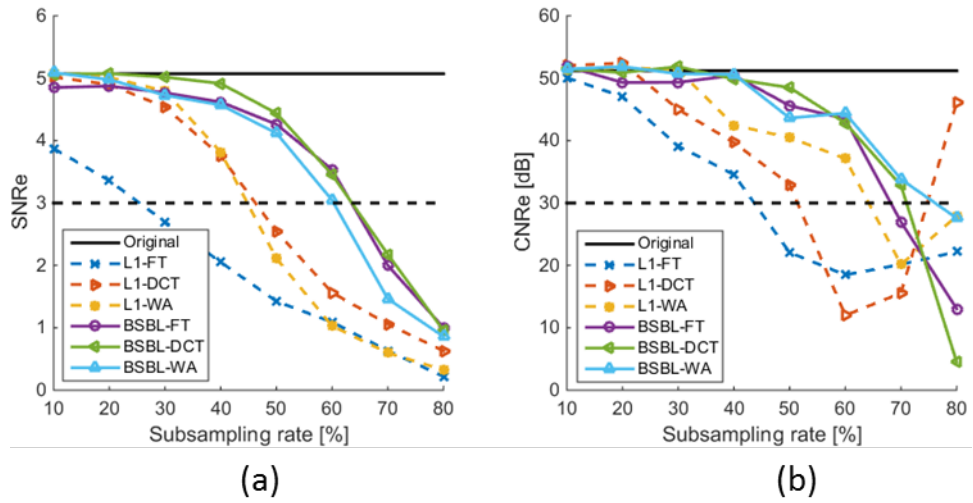


Figure 13. (a) SNRe and (b) CNRe of the elastograms as a function of subsampling rate. The image quality measures are computed on the elastograms produced from the original data and from various CS reconstruction frameworks.

Table 1. Parameters for numerical phantoms

Parameter	Echoic phantom	Elastography phantom
Phantom size	50×10×55 mm ³	40×50×10 mm ³
Center frequency	3.5 MHz	3.5 MHz
Sampling frequency	28 MHz	28 MHz
Width	0.44 mm	0.44 mm
Height	5 mm	5 mm
Kerf	0.022 mm	0.022 mm
Number of elements	192	152
Tx elements	64	24
Rx signals considered	128	128
Tx/Rx focus	50 mm	50 mm

Table 2. Image quality measures, CPU time, and average number of iteration at the threshold subsampling rate(SR) associated with various CS reconstruction frameworks.

CS reconstruction	CS model basis	Threshold SR(%)	MAE	SNRe	CNRe (dB)	CPU (sec)	Avg. iteration
L1	FT	40	1.899e-4	2.052	34.564	105.91	42.61
L1	DCT	40	1.312e-4	3.754	39.694	28.492	12.95
L1	WA	40	1.216e-4	3.817	42.474	16.731	12.73
BSBL	FT	60	1.369e-4	3.534	43.489	55.479	7
BSBL	DCT	60	9.538e-5	3.455	42.839	41.864	7
BSBL	WA	60	1.681e-4	3.045	44.391	38.454	7